Received: 13 March 2024 | Revised: 3 June 2024 | Accepted: 25 November 2024 | Published online: 6 December 2024

Journal of Optics and Photonics Research
2025, Vol. 2(2) 67–76
DOI: 10.47852/bonviewJOPR42022826
BON VIEW PUBLISHING

RESEARCH ARTICLE

Fiber Bragg Grating-Based Tunable Wavelength Orbital Angular Momentum Beam Generation with Varying Polarization

Avijit Koley[1,*]

[1]*Department of Electronic Engineering, National Taiwan University of Science and Technology, Taiwan, Province of China*

Abstract: This paper introduces and theoretically analyzes the generation of orbital angular momentum (OAM) modes with different polarization in a few-mode optical fiber using short-period gratings (Bragg gratings) at telecommunication wavelengths. The modal characteristics of the supported modes have been studied using a full-vector true-mode analysis. Additionally, an appropriately designed raised-cosine apodized grating is employed to couple the HE_{11} core mode to the counter-propagating cladding mode. In contrast to the long-period grating-based OAM mode generation, the present scheme is free from periodic back-coupling of optical power into the fundamental core mode which drastically enhances the OAM mode purity. The ±1-order OAM beam has been generated by combining the first higher-order core modes with a $\pi/2$ phase shift between them. This paper also shows that by combining different higher-order modes, it is possible to obtain a linearly polarized OAM mode or a circularly polarized OAM mode. Finally, I also report that in fibers with larger core radius, the higher-order OAM mode of topological charge ±2 or higher can also be generated using a similar approach of using short-period gratings. The topological charge of the OAM mode is verified by observing both the coaxial and off-axial interference fringes.

Keywords: orbital angular momentum, vector modes, optical vortex, fiber Bragg grating, few-mode fiber

1. Introduction

An optical vortex is a common type of structured light, which can be broadly categorized into two types: phase vortex and polarization vortex [1–3]. Polarization vortices are generated when the polarization direction is completely undetermined at the beam center, leading to a polarization singularity at the beam center. The polarization characteristics of a cylindrical vector beam (CVB) correspond to those of a vortex beam. The other vortex beam is characterized by having a helical wavefront of $exp(il\phi)$, where ϕ is the azimuthal angle, and l is the topological charge, in which the phase is completely undetermined at the beam center. The intensity profile of both of these vortex beams, polarization as well as phase vortex, exhibits a doughnut shape with a central dark region. The discovery made by Allen et al. [4] in 1992 that beams with a helical phase front $exp(il\phi)$ have orbital angular momentum (OAM) of $l\hbar$ per photon was a major breakthrough in our knowledge of the characteristics and uses of optical vortices. The phase vortex beams, also known as OAM modes, have wide range of applications across different fields, e.g., in optical micro-manipulation [5, 6], optical imaging [7], quantum optics [8], optical tweezers [9, 10], nonlinear optics [11, 12], nano-scale microscopy [13, 14], etc. Very recently, due to their unique properties, the OAM beam has attracted great attention in developing novel multiplexing techniques increasing the data carrying capacity of optical channels [15–19]. To generate OAM beams, several methods have been devised, such as spiral phase plate [20–23], computer-generated holograms [24–26], microresonator or subwavelength grating [23, 27–31], helically twisted fiber [32, 33].

Majority of OAM beam generation and conversion techniques are primarily based on discrete components, and the associated complexity of optical alignment makes them difficult to use in compact, low-loss systems as well as in long-distance systems. Recent research advances have made it possible to generate and guide vortex beams in optical fiber, which has considerably reduced the external interference and increased the transmission efficiency, raising a lot of research interest to explore novel fiber designs for OAM beam generation. For OAM mode generation in commercial optical fibers with conventional step-index profile, typically the initial step involves exciting the first few guided modes at the fiber's input end, and then, the appropriate mode coupling is achieved through the utilization of fiber gratings and/or fiber modeselective couplers. Among various mode coupling techniques, the optical fiber grating-based technique has attracted much attention in the process of generating OAM, owing to the availability of the matured grating fabrication technology, possibility of high-speed volume reproducibility of gratings, and the freedom they offer in tailoring the transmission spectra of pre-selected guided modes. Numerous studies, both the theoretical and experimental, have been conducted to demonstrate how to generate an OAM mode and switch between the OAM modes in fiber using acoustically induced LPFG [34, 35], mechanical long-period fiber grating [36], long-period grating [37], fiber Bragg grating [38–41], helical Bragg grating technology [42], helical

---

[*]**Corresponding author:** Avijit Koley, Department of Electronic Engineering, National Taiwan University of Science and Technology, Taiwan, Province of China. Email: avkoley@mail.ntust.edu.tw

long-period fiber grating [43], multi-ring air-core fiber [44], helically twisted hollow-core antiresonant fiber [45].

The LPFG-based OAM beam generation technique has its own advantages and inherent shortcomings, e.g., the OAM beam suffers badly due to the (*i*) inherent cross-sensitivity of the LPFG to a number of external perturbation parameters, and (*ii*) a slight mismatch in the grating length of LPFG leading to the back-coupling of optical power from the vortex beam to the fundamental mode of the fiber, reducing the mode purity. The LPFGs are much more sensitive to external perturbations, such as temperature, strain, refractive index, and so on, than the fiber Bragg gratings (FBGs) [46]. Furthermore, it is well known that the transmission spectrum of LPFG varies periodically with grating length. Now, since all the supported modes of a few-mode fiber already carry some energy right through the launching end (determined by the spot-size overlap of the optical source with various guided modes), a precise control on the LPFG length is needed to ensure high mode purity of the generated OAM beam. A slight increase in the grating length from the precise grating length needed for 100% power coupling would lead to power coupling back from LP_{11} mode to the fundamental mode, leading to reduced mode purity of OAM beam. On the other hand, a slight decrease in the grating length from the precise grating length needed for 100% power coupling would anyway result in poor mode purity of the OAM beam. So, even if the other perturbation parameters remain constant and the grating length varies, the power would couple from fundamental mode to target mode and again coupled back to the fundamental mode [47]. Thus, the grating length must be chosen very carefully in co-propagating coupling. On the other hand, in the case of FBG, the mode coupling increases with grating length and then starts saturating after a certain length, without power being coupled back to the fundamental mode [46].

In this paper, I present a counter-propagating cladding mode-assisted model for generating OAM mode in optical fiber. Contrary to the conventional FBGs, the counter-propagating cladding mode-based grating designs have added advantages of not requiring any circulator or bulky prism to re-route the reflected mode, which in general is needed to avoid the backreflected mode from damaging the input laser cavity. The backward-propagating cladding mode quickly gets absorbed by the polymer coating of the fiber. In this model, I have considered a two-mode fiber, where the fundamental core mode ($HE_{11}^{x/y}$ vector mode), and the first higher-order nearly degenerate modes (TE_{01}, $HE_{21}^{even/odd}$ and TM_{01} vector modes) are excited. These vector modes correspond to the LP_{01} and LP_{11} modes in scalar mode approximation. A suitably designed uniform FBG is considered inside the fiber core region in order to reflect the fundamental mode by coupling with the symmetric order cladding mode. I have then shown that circularly polarized OAM (CP-OAM) mode or linearly polarized OAM (LP-OAM) mode of ±1-order can be generated by combining remaining higher-order vector modes by introducing an appropriate phase shift between the participating modes.

2. Model and Theory

The generation of OAM modes is commonly achieved by combining higher-order degenerate vector modes or scalar modes with a phase difference of $\frac{\pi}{2}$. Consider two-mode fiber which, under weakly guiding approximation, can support LP_{01} and LP_{11} modes. LP_{01} mode represents the $HE_{11}^{x/y}$ vector mode, and the first higher-order mode LP_{11} represents quadruply degenerate vector modes, namely TE_{01}, $HE_{21}^{even/odd}$, and TM_{01} vector modes.

Although many research groups have presented various approaches to generate OAM mode, but nearly all of those studies construct the vector modes using *LP* modes [1, 36, 48]. The LP_{lm} modes ($l > 0$) have degenerate even and odd forms. OAM mode in optical fiber with topological charge (also called order of OAM mode) 1 can be generated by superposing the degenerate LP_{lm} modes with $\pm\frac{\pi}{2}$ phase difference.

$$OAM_{\pm l} = LP_{lm}^{even} \pm i\, LP_{lm}^{odd} \tag{1}$$

However, *LP* modes do not represent the true eigenmodes of a fiber. To accurately determine the mode field distribution in an optical fiber, a comprehensive vector modal analysis is required. In spite of this, most of the studies use approximate scalar modes with the following transverse electric field distributions [1, 3] to obtain OAM mode in fiber,

$$E(r,\phi) = F_{lm}(r)\ \Phi(l\phi) \tag{2}$$

A thorough explanation of the notation for different order vector modes as defined in Equation (2), along with their respective field orientations, is discussed in Ramachandran and Kristensen [1], Ma et al. [2] and Mao et al. [3].

To investigate the generation of OAM modes in optical fibers comprehensively, a full vectorial approach, devoid of any approximate modes, is considered in this study. For an optical fiber, the longitudinal field components satisfy the following differential equations,

$$\frac{\partial^2\Psi}{\partial r^2} + \frac{1}{r}\frac{\partial^2\Psi}{\partial r^2} + \frac{1}{r^2}\frac{\partial^2\Psi}{\partial\phi^2} + [k_0^2 n^2(r) - \beta^2]\Psi = 0 \tag{3}$$

where $\Psi = E_z$ and H_z, k_0 is the free space propagation constant, the distribution of refractive index is expressed by $n(r)$, and β is the propagation of the particular mode. The longitudinal field component distribution for even core mode, HE_{mn}^{even}, across the various regions of the optical fiber is well described in Snyder and Love [49],

$$\begin{aligned} E_z(r,\phi) &= A_c J_m(\kappa_c r)\cos(m\phi) \qquad \mathit{for}\quad 0 \le r \le a \\ &= B_c K_m(\gamma_c r)\cos(m\phi) \qquad \mathit{for}\quad r \ge a \end{aligned}$$

and

$$\begin{aligned} H_z(r,\phi) &= C_c J_m(\kappa_c r)(-\sin(m\phi)) \qquad \mathit{for}\quad 0 \le r \le a \\ &= D_c K_m(\gamma_c r)(-\sin(m\phi)) \qquad \mathit{for}\quad r \ge a \end{aligned} \tag{4}$$

Similarly, for odd mode, HE_{mn}^{odd}, the solutions are taken as,

$$\begin{aligned} E_z(r,\phi) &= A_c J_m(\kappa_c r)\sin(m\phi) \qquad \mathit{for}\quad 0 \le r \le a \\ &= B_c J_m(\gamma_c r)\sin(m\phi) \qquad \mathit{for}\quad r \ge a \end{aligned}$$

and

$$\begin{aligned} H_z(r,\phi) &= C_c J_m(\kappa_c r)\cos(m\phi) \qquad \mathit{for}\quad 0 \le r \le a \\ &= D_c J_m(\gamma_c r)\cos(m\phi) \qquad \mathit{for}\quad r \ge a \end{aligned} \tag{5}$$

where $\kappa_c = k_0\sqrt{n_c^2 - n_{eff}^2}$ and $\gamma_c = k_0\sqrt{n_{eff}^2 - n_{cl}^2}$. The transverse field components are then obtained from axial field components using Maxwell's curl equations [49, 50].

In the full vectorial method, the transverse electric field of the HE_{mn} mode can be represented as follows:

$$HE_{mn}^{even} = E_r^{even}(r,\phi)\hat{r} + E_\phi^{even}(r,\phi)\,\widehat{\phi}$$

$$= [E_r^{even}(r,\phi)\,\cos(\phi) - E_\phi^{even}(r,\phi)\,\sin(\phi)]\widehat{x}$$

$$+ [E_r^{een}(r,\phi)\,\sin(\phi) + E_\phi^{even}(r,\phi)\,\cos(\phi)]\widehat{y} \qquad (6)$$

Similarly, the expression of electric field for odd HE_{mn} mode, TE_{0n} mode, and TM_{0n} mode can also be written [49].

Thus, we see that the vortex mode with ±1 order can be obtained by linearly combining the different vector modes like HE_{21}^{even} and HE_{21}^{odd}, or HE_{21}^{odd} and TE_{01}, or HE_{21}^{even} and TM_{01}. Higher-order (±2) vortex mode can also be generated using a combination of HE_{31}^{even} and HE_{31}^{odd} modes or EH_{11}^{even} and EH_{11}^{odd} modes. The ±1 order vortex mode has the following form:

$$OAM_{\pm 1} = HE_{21}^{even} \pm i\; HE_{21}^{odd}$$

$$= HE_{21}^{odd} \pm i\; TE_{01}$$

$$= HE_{21}^{even} \pm i\; TM_{01} \qquad (7)$$

To verify that the resultant beam carries orbital angular momentum (OAM), an interference (either coaxial interference or an off-axial interference) between the generated vortex beam and a reference Gaussian beam is performed. And by examining the resulting interference pattern, the topological charge (also called order of OAM mode) of the corresponding vortex beam can be determined.

3. Result and Discussion

3.1. Vortex mode generation

In this section, we will discuss the OAM mode generation in fiber by looking at two different configurations (*i*) for circularly polarized OAM (CP-OAM) mode generation and (*ii*) for linearly polarized OAM (LP-OAM) mode generation. In this analysis, the fiber under consideration comprises an outer cladding region made of silica and a core region doped with 3.1 mole % of GeO_2 in SiO_2, with a radius of 6 μm and index contrast of 0.0047 has a V-number of ~2.83 at wavelength of 1550 nm. The fiber diameter is set to 12 μm so that it can theoretically support six vector modes: $HE_{11}^{x/y}$, TE_{01}, $HE_{21}^{even\ odd}$, and TM_{01}. By coherently combining these vector modes, this fiber can theoretically support six OAM modes, as seen in Equation (4), associated with ±1 topological charge.

A uniform Bragg grating [47] is written inside the core region. It is well known that the fundamental HE_{11} mode is not a vortex mode [1]. Since OAM is not carried by the fundamental HE_{11} mode, its existence just makes the OAM mode purity worse. Therefore, the undesirable HE_{11} mode can be reflected back with the aid of a Bragg grating by coupling it with a core mode or cladding mode, which will be discussed in detail in section 3B.

3.1.1. Circularly polarized OAM mode generation

Here we numerically analyze the OAM mode with topological charge $l = \pm 1$ by numerically setting a $\frac{\pi}{2}$ phase difference between two degenerate HE_{21} modes. Because the HE_{21} modes are orthogonally polarized, the OAM modes that are generated will be circularly polarized.

$$OAM_{\pm 1} = HE_{21}^{even} \pm i\; HE_{21}^{odd} \qquad (8)$$

The intensity and phase distributions of the generated OAM beam are illustrated in Figure 1. The annular intensity pattern with polarization of HE_{21} mode can be clearly seen in Figure 2. Interference between the generated annular beam and a spherical Gaussian beam has been investigated to confirm whether it is a vortex beam or not. Figure 1(a) and (b) show the interference patterns of annular-shaped beam and reference beam. As can be seen, the interference pattern is a spiral, which indicates that the annular beam is a vortex beam. The topological charge of the vortex beam (order of the OAM mode) can be determined by counting the number of spiral rotations. The single spiral interference pattern as shown in Figure 1(a) and (b) clearly indicates the OAM_{-1} (clockwise) and OAM_{+1} (counterclockwise) mode, respectively. The phase distribution of superposed two degenerate HE_{21} mode is displayed in Figure 1(c) and (d). The rotation of the phases also indicates that the doughnut-shaped beam is a vortex beam with a topological charge $l = \mp 1$, as the phase rotates only one time over 2π. When we interfere the vortex beam with an off-axial plane wave, we can see a fork-like fringe pattern; this is another signature of vortex beam. The interference pattern between the vortex beam and the reference plane wave is depicted in Figure 1(e) and (f). It can be seen from these figures that the interference pattern of the vortex beam and the plane wave are forked like fringes, the number of the branch in each of these figures is one which equals the topological charge of the vortex beam.

The coherent superposition of even and odd HE_{21} modes with a $\frac{\pi}{2}$ phase direction yields the circularly polarized OAM 1st-order mode. By twisting or lateral squeezing the fiber, one can achieve this phase delay between the degenerate modes. In literature, a number of very innovative methods for generating $\frac{\pi}{2}$ phase difference between fiber modes have been reported. McGloin et al. [51] have proposed a straightforward approach to induce the phase difference by applying stress to the fiber using rectangular lead weights. Li et al. [36] have demonstrated that the phase difference can be obtained by using a rotator and a flat slab. Here, we can realize the $\frac{\pi}{2}$ phase difference between the HE_{21} even and odd modes by launching circularly polarized (CP) light at the input end of the fiber. To generate the CP state of the input light, a polarizer and quarter wave plate are used together.

3.1.2. Linearly polarized OAM mode generation

It is also possible to obtain the linearly polarized $OAM_{\pm 1}$ modes by combining the other distinct vector modes defined in Equation (4) (last 2 row). Among the four higher-order mode, HE_{21}^{even} and HE_{21}^{odd} are strictly degenerated, having orthogonal polarization states and the exact same effective refractive index, but the TE_{01} and TM_{01} mode have slightly different effective indices. The simulated effective indices of the vectors modes can be calculated as 1.44693224 (HE_{11}), 1.44460120 (TE_{01}), 1.44460061 (HE_{21}), and 1.44459877 (TM_{01}) at wavelength of 1550 nm. As we can see, the index difference between adjacent first higher-order vector modes is $\Delta n_{TE-TM} \sim\ 6 \times 10^{-7}$ and $\Delta n_{HE-TM}\ \sim\ 1.84 \times 10^{-7}$, which is extremely small. With an inadequate index difference ($\Delta n \sim 10^{-5}$), we can claim that the two modes remain degenerate. It is well known that TE and TM modes coexist alongside HE_{21} modes in multimode fiber. Because their index difference is so small, they will pair to generate a linearly polarized mode at the output. The field distributions of TE_{01}, HE_{21}^{even}, HE_{21}^{odd}, TM_{01} modes are depicted in Figure 2 along with the field distribution of linearly polarized (LP_{11}) mode formed by superposing of HE_{21}^{odd} and TE_{01}, and

Figure 1
Coaxial interference pattern of (a) OAM$_{-1}$ and (b) OAM$_{+1}$ with a reference Gaussian beam. Phase pattern of generated (c) OAM$_{-1}$ and (d) OAM$_{+1}$. Off-axial interference pattern of (e) OAM$_{-1}$ and (f) OAM$_{+1}$ with Gaussian beam

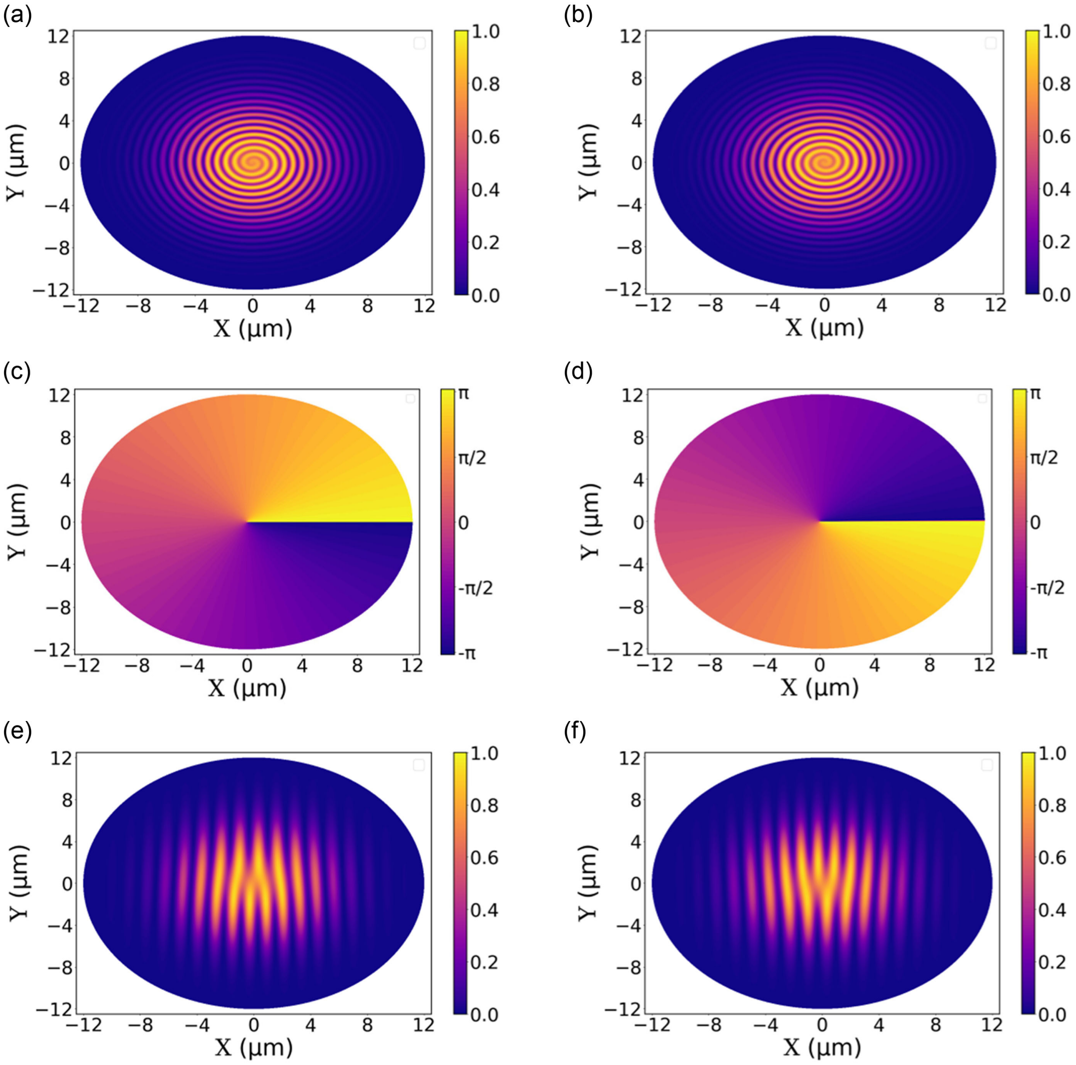

Figure 2
Top row (a and b): Modal intensity pattern and polarization distribution of first higher-order vector modes: HE_{21}^{odd}, TE_{01}, HE_{21}^{even}, and TM_{01}. Bottom row (a and b): Intensity and polarization distribution of the mixing vector modes

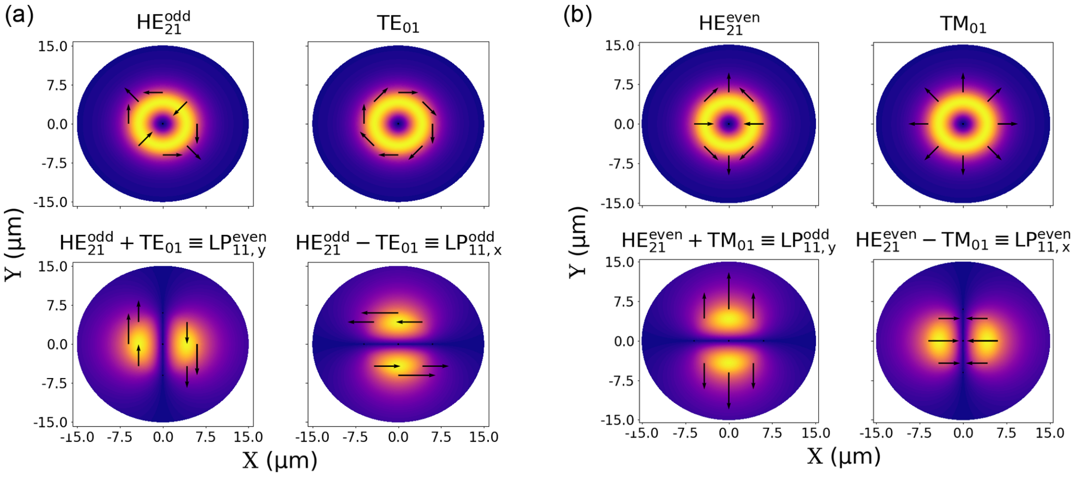

HE_{21}^{even} and TM_{01}. So, their linear combination (see last 2 rows, Equation (4)) generates linearly polarized vortex beam.

However, introducing a π/2 phase delay between them is critical. Since the fundamental mode, HE_{11}, does not carry OAM, the technique that presented in this model is that to reflect this undesirable HE_{11} mode by coupling it to the backward-propagating cladding mode with a very narrow bandwidth at a predetermined wavelength. Within this bandwidth, we have TE_{01}, HE_{21}, and TM_{01} at the output (transmission) end. When the phase difference between the modes is $\frac{\pi}{2}$, the OAM modes will be generated. And the phase difference between modes, $\Delta\phi$, is defined by the mode propagation constant β as well as the length of the fiber,

$$\Delta\phi = (\beta_{HE21} - \beta_{TE01}) \times L \tag{9}$$

where L is the fiber length and m can be any integer $m = 0, 1, 2, \ldots$ Therefore, the $\Delta\phi$ between the modes can be controlled by varying the fiber length, and as long as it is $(m + 1/2)\pi$, the ±1-order LP-OAM modes will be at the output, transmission end. Here, as an example, I have plotted Figure 3 for x polarized OAM_{+1} light, and the same procedure can be used for other linear polarization states as well. As an illustration, the equation for x polarized OAM_{+1} generated by the combination of TE_{01} and HE_{21}^{odd} is written as

$$OAM_{+1}(\hat{x}) = HE_{21}^{odd} - i\, TE_{01} \tag{10}$$

The well-known signature interference pattern of the generated OAM mode for the combination TE_{01} and HE_{21}^{odd} is plotted in Figure 3(a). The corresponding phase distribution is also plotted in the same figure (Figure 3(b)). The same can also be obtained for other combination as mentioned in Equation (4) (last 2 rows).

3.2. Fiber Bragg grating

Fiber Bragg gratings (FBG) are reflecting grating that are used for counter-directional modal coupling between guided modes of optical fiber [47, 52]. Their operational principle is based on (*i*) the phase matching between the coupled modes, and (*ii*) modal overlap between those modes over the grating region. The phase matching condition is given by Kashyap [47],

$$\left(\beta_{eff}^{\mu} + \beta_{eff}^{\nu} + \kappa_{\mu-\mu} + \kappa_{\nu-\nu}\right) \times \Lambda = 2\pi \tag{11}$$

where β_{eff}^{x} is the effective index of mode x, and κ_{x-x} is the self-coupling coefficient of mode x. The wavelength at which the resonance coupling occurs is given as

$$\lambda_R = \frac{\left(n_{eff}^{\mu} + n_{eff}^{\nu}\right)}{\frac{1}{\Lambda} - \frac{\kappa_{\mu-\mu}+\kappa_{\nu-\nu}}{2\pi}} \tag{12}$$

Here, n_{eff}^{μ} and n_{eff}^{ν} are the effective refractive indices ($n_{eff}^{x} = \frac{\beta_{eff}^{x}}{k_0}$) of the two coupled modes, respectively, and k_0 is the free space propagation constant. In the grating region, the core refractive index gets modified as,

$$n_c(z) = n_c\left[1 + \sigma(z)\left\{1 + \cos\left(\frac{2\pi}{\Lambda}z\right)\right\}\right] \tag{13}$$

In this simulation, the considered fiber with a core diameter of 12 microns supports the fundamental mode (HE_{11}) and first higher-order mode group (TE_{01}, TM_{01}, and HE_{21}). Since the fundamental HE_{11} mode does not carry OAM, its presence only worsens the OAM mode purity. To improve OAM mode purity we can (*i*) either redirect power from HE_{11} mode to OAM-carrying HE_{21} mode, or (*ii*) reflect back the HE_{11} mode. The first option, i.e., coupling power between HE_{11} and HE_{21} modes, requires extremely high control over the grating length as co-directional coupling (LPG-based coupling) is always associated with periodic power coupling between the coupled modes (see Figure 4), resulting in deteriorated OAM mode purity. Two possibilities might arise: (*a*) grating length is smaller than the optimum length, resulting in some power still carried by HE_{11} mode, or (*b*) grating length is larger than the optimum length, resulting in power coupled back to HE_{11} mode from the HE_{21} mode. Further, since the co-directional modal coupling is extremely sensitive to external perturbations as compared to the counter-directional modal coupling [46], a slight change in the environmental conditions might jeopardize the delicate grating length requirements. Contrast to the co-directional coupling, the counter-directional coupling (FBG-based coupling) is (*i*) free from periodic recouping of power, and (*ii*) relatively weakly influenced by environmental perturbations.

As previously stated, the Bragg grating is a reflecting grating that can be used to couple power between counter-propagating modes. As a result, we can selectively reflect the undesirable mode using FBG at the point of need. In this simulation, I used a uniform non-tilted Bragg grating with a grating strength of

Figure 3

(a) Interference pattern and (b) phase pattern of generated OAM_{+1} mode for HE_{21}^{odd}- i TE_{01}

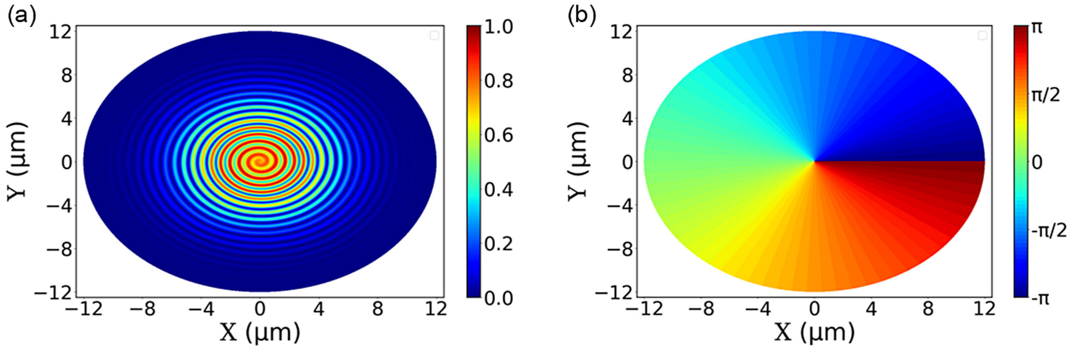

Figure 4
Variation of transmission of LPG (blue) and reflection of FBG (green) with grating length

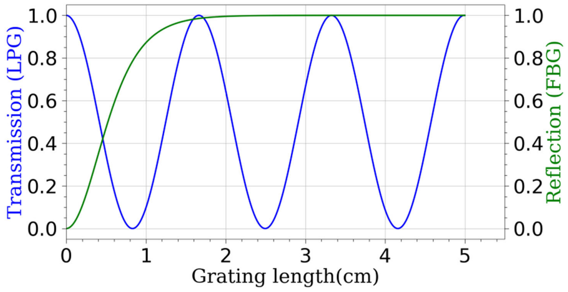

$\sigma_0 = 10^{-4}$; σ is related to maximum RI perturbation (Δn) in the grating region via $\Delta n = \sigma n_{co}$. As we know, the symmetric gratings couple modes with the same azimuthal numbers; therefore, the fundamental core mode which has $m = 1$ can be coupled to the counter-propagating cladding mode HE_{1n} modes. For the optical fiber parameters used in this study, the required grating period is $\Lambda = 0.543\ \mu m$ to get a Bragg reflection at $1.55\ \mu m$, caused by grating assisted resonant excitation of counter-propagating HE_{19} cladding mode. In Figure 5(a), we have plotted the transmission spectrum corresponding to HE_{11} core mode – HE_{19} cladding mode coupling (red curve) and HE_{21} core mode – HE_{19} cladding mode coupling (blue curve). As expected, no resonance is observed corresponding to the HE_{21} core mode – HE_{19} cladding mode coupling, which matches with our predictions. Fiber Bragg gratings with uniform refractive index modulation exhibit a series of sidelobes at both sides of the Bragg wavelength, as shown in Figure 5(a). These sidelobes appear in the reflection spectrum due to abrupt changes in the RI profile at the grating boundaries. Therefore, it is essential to minimize and, if at all feasible, eliminate these sidelobes in order to have low sidelobe suppression (SLS) ratio. This means that as the sidelobes become less prominent, there is a clearer and more prominent reflection peak. This is particularly advantageous in applications requiring high spectral purity, such as wavelength division multiplexing (WDM) systems, high-precision sensors, and others. Decreased sidelobe levels lead to a cleaner signal with less interference from neighboring channels, thereby improving the signal-to-noise ratio. The grating apodization, which is a variation of RI modulation strength along the grating length, is a very well-known technique used to reduce the sidelobes. Apodization involves a gradual tapering of the refractive index modulation, which mitigates abrupt transitions, resulting in a significant suppression of sidelobes. In this simulation, I have used a raised-cosine apodized grating profile which has the following form for its grating strength,

$$\sigma(z) = \sigma_0 \cos\left(\frac{\pi\left(z - \frac{L}{2}\right)}{L}\right) \tag{14}$$

Figure 5(b) shows the transmission spectra of uniform period FBG with raised-cosine apodization profile. Changing the amplitude modulation depth has a notable impact on the spectral properties and performance of the Bragg grating, including (i) Reflectivity, (ii) Bandwidth, and (iii) sidelobe Suppression. Higher modulation depths correspond to greater refractive index changes, resulting in stronger reflection peaks and larger bandwidth, but can also elevate sidelobe levels. A tradeoff will exist between sidelobes and high modulation depth. Therefore, the apodized grating has been considered in order to have high reflectivity while minimizing sidelobe levels. As can be seen, the sidelobe is suppressed and ripples are reduced. As the fundamental mode is coupled to a backward-propagating cladding mode by FBG, a

Figure 5
Transmission spectrum for HE_{11} core mode-HE_{19} cladding mode coupling (red) and HE_{21} core mode-HE_{19} cladding mode coupling (blue) (a) without apodization and (b) with pure cosine apodization. Intensity of (HE_{21} + HE_{11}) at the (c) resonance wavelength and (d) at the edge of the transmission point of bandwidth

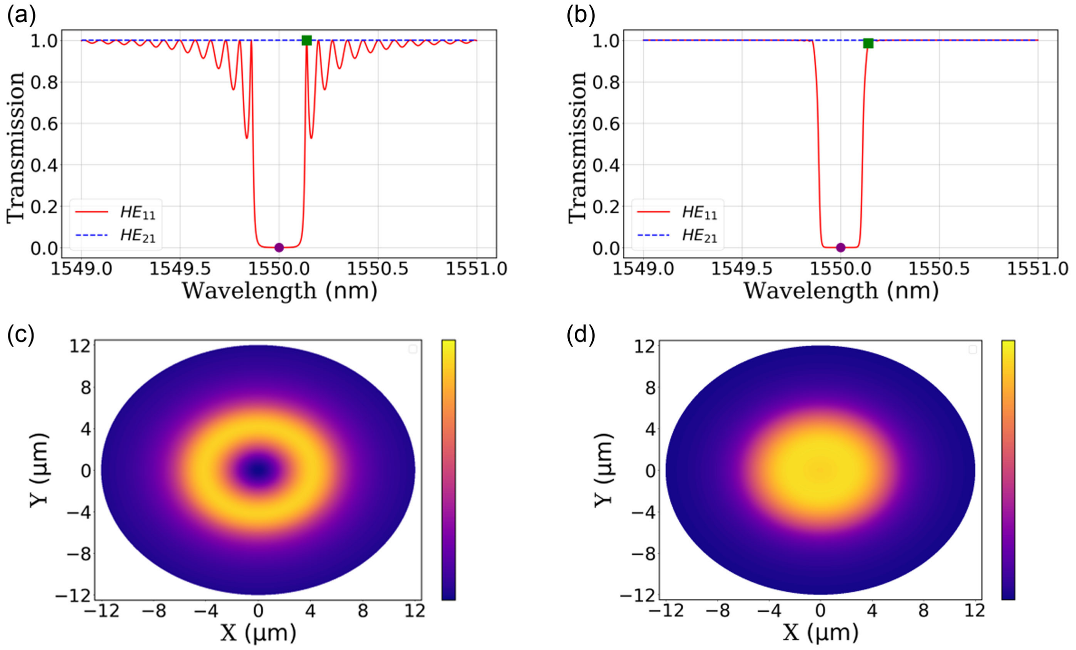

doughnut-shaped intensity profile is anticipated at the output end. As we approach the band edge, the presence of the HE_{11} mode leads to the gradual fading of the distinctive doughnut-shaped intensity profile. Here, we would like to mention that the bandwidth of high mode purity OAM mode can be broadened by increasing the grating strength and/ or, more preferably, by using appropriately chirp Bragg gratings. The cumulative intensity profile of HE_{11} mode + HE_{21} mode at two different wavelengths: one at the dip of the transmission spectra (maroon circle in Figure 5(a)) and the other at the transmission edge point (green square in Figure 5(a)) are shown in Figure 5(c) and (d), respectively. The annular shape clearly shows that only HE_{21} mode exists at the flattened resonance wavelength around 1.55 μm, whereas the Gaussian-like intensity profile indicates that both HE_{21} and HE_{11} modes exist outside the grating bandwidth at the output end.

To have a purely HE_{21} mode, we must also suppress the *TE* and *TM* modes, which can be accomplished by coupling the forward-propagating *TE* and *TM* modes to counter-propagating cladding *TE* and *TM* modes by employing two additional uniform gratings with the appropriate grating period. Here, I would like to mention that reflecting unwanted core modes by means of coupling those to counter-propagating core modes, would risk damaging the light source at the input end of the fiber. In contrast to this, the energy coupled to the counter-propagating cladding modes is dissipated by absorption in the fiber jacket and therefore in this analysis, I have considered power coupling to a higher-order cladding mode.

3.3. Verification of the model

Using a similar approach, OAM mode with higher order can also be generated. To show that the even and odd combination of HE_{mn} mode can produce OAM mode of order $l = m - 1$ (also called topological order l), I carried out the same procedure for HE_{11}, $HE_{21,}$ and HE_{31} modes. In order to support many guided modes, in the subsequent study we have considered fiber with a core radius of 9.6 μm. The intensity distribution and the interference pattern for each generated OAM mode of order l are plotted in Figure 6. The intensity and coaxial interference of HE_{11} mode have been shown in Figure 6(a) and (b), respectively. We can see that no spiral fringes are observed, which indeed imply that HE_{11} mode has zero topological charge, $l = 1 - 1 = 0$, which also indicates that HE_{11}

Figure 6

Intensity distribution of (a) HE_{11}, (c) $HE_{21,}$ and (e) HE_{31} core modes. Interference pattern of OAM$_{+l}$ for (b) HE_{11}^{even} + iHE_{11}^{odd} (d) HE_{21}^{even} + iHE_{21}^{odd} and (f) HE_{31}^{even} + iHE_{31}^{odd}

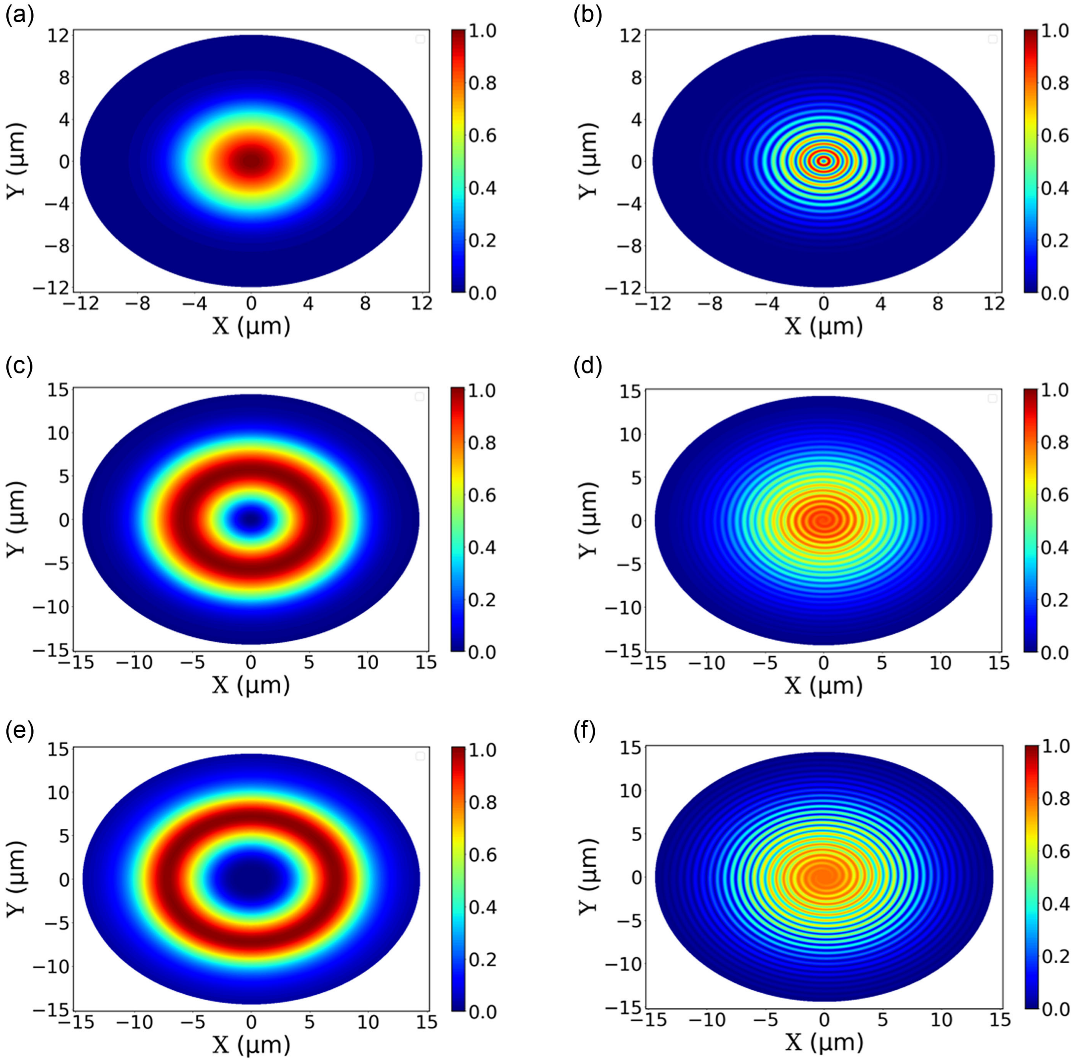

does not carry OAM. The doughnut-like shape in Figure 6(c) and (e) clearly indicates the higher topological order ($l = 1$ and $l = 2$) OAM-carrying modes HE_{21} and HE_{31}, which can be verified by looking into the interference pattern.

We can see that the higher the azimuthal number, the wider the central dark region. In addition, the corresponding interference patterns are depicted in Figure 6(d) and (f), respectively. The single spiral in Figure 6(d) confirms that the generated mode is a vortex mode of order $l = 2 - 1 = 1$ while the double spiral in Figure 6(f) clearly shows the output mode is a second-order ($l = 3 - 1 = 2$) vortex mode.

4. Conclusion

An analysis of OAM-carrying modes in optical fiber has been presented using the true vector modal analysis of a few-mode optical fiber. In contrast to the widely used artificial construction of vector modes using the approximate *LP* modes, this study is based on exact vector modes: *TE*, *TM*, and *HE* modes of the optical fiber. An appropriately designed raised-cosine apodized Bragg grating is considered to reflect back the undesirable HE_{11} core mode by coupling it to counter-propagating cladding mode and a $\frac{\pi}{2}$ phase shift between the appropriate modes has been considered for OAM mode generation. In contrast to the long-period grating-based OAM mode generation, the present scheme is free from periodic back-coupling of optical power into the fundamental core mode, thereby drastically enhancing the OAM mode purity over the grating wavelength window. By combining different higher-order modes we have obtained both the linearly polarized OAM mode as well as the circularly polarized OAM mode. Finally, I have also shown that in fibers with larger core radius, the higher-order OAM mode of topological charge ±2 or higher can also be generated using a similar approach. The topological charge of the OAM mode has been verified by observing both the coaxial as well as off-axial interference fringes. Our model is relatively straightforward as it consists of standard fiber gratings instead of specially designed fibers such as ring-shaped fibers or other complex designs, as mentioned in the introduction.

Ethical Statement

This study does not contain any studies with human or animal subjects performed by the author.

Conflicts of Interest

The author declares that he has no conflicts of interest to this work.

Data Availability Statement

Data sharing is not applicable to this article as no new data were created or analyzed in this study.

Author Contribution Statement

Avijit Koley: Conceptualization, Methodology, Software, Validation, Formal analysis, Data curation, Writing – original draft, Writing – review & editing.

References

[1] Ramachandran, S., & Kristensen, P. (2013). Optical vortices in fiber. *Nanophotonics*, *2*(5–6), 455–474. https://doi.org/10.1515/nanoph-2013-0047

[2] Ma, M., Lian, Y., Wang, Y., & Lu, Z. (2021). Generation, transmission and application of orbital angular momentum in optical fiber: A review. *Frontiers in Physics*, *9*, 773505. https://doi.org/10.3389/fphy.2021.773505

[3] Mao, D., Zheng, Y., Zeng, C., Lu, H., Wang, C., Zhang, H., . . . , & Zhao, J. (2021). Generation of polarization and phase singular beams in fibers and fiber lasers. *Advanced Photonics*, *3*(1), 014002. https://doi.org/10.1117/1.AP.3.1.014002

[4] Allen, L., Beijersbergen, M. W., Spreeuw, R. J. C., & Woerdman, J. P. (1992). Orbital angular momentum of light and the transformation of Laguerre-Gaussian laser modes. *Physical Review A*, *45*(11), 8185–8189. https://doi.org/10.1103/PhysRevA.45.8185

[5] Ng, J., Lin, Z., & Chan, C. T. (2010). Theory of optical trapping by an optical vortex beam. *Physical Review Letters*, *104*(10), 103601. https://doi.org/10.1103/PhysRevLett.104.103601

[6] Qiu, S., Wang, C., Liu, T., & Ren, Y. (2022). Generation of spiral optical vortex with varying OAM for micro-manipulation. *Optics Communications*, *524*, 128767. https://doi.org/10.1016/j.optcom.2022.128767

[7] Zeng, J., Dong, Y., Wang, Y., Zhang, J., & Wang, J. (2023). Optical imaging using orbital angular momentum: Interferometry, holography and microscopy. *Journal of Lightwave Technology*, *41*(7), 2025–2040. https://doi.org/10.1109/JLT.2022.3225214

[8] Liu, S., Lou, Y., & Jing, J. (2020). Orbital angular momentum multiplexed deterministic all-optical quantum teleportation. *Nature Communications*, *11*(1), 3875. https://doi.org/10.1038/s41467-020-17616-4

[9] Padgett, M., & Bowman, R. (2011). Tweezers with a twist. *Nature Photonics*, *5*(6), 343–348. https://doi.org/10.1038/nphoton.2011.81

[10] Ren, W., Gong, Y., Zhang, Z., & Li, K. (2021). Optical OAM tweezer based on graded-index multimode fibers. *Applied Optics*, *60*(25), 7634–7639. https://doi.org/10.1364/AO.431057

[11] Buono, W. T., & Forbes, A. (2022). Nonlinear optics with structured light. *Opto-Electronic Advances*, *5*(6), 210174. https://doi.org/10.29026/oea.2022.210174

[12] Chen, S., Ma, T., Yu, Q., Chen, P., Yang, X., Wu, X., . . . , & Zhang, Y. (2023). A perspective on the manipulation of orbital angular momentum states in nonlinear optics. *Applied Physics Letters*, *122*(4), 040503. https://doi.org/10.1063/5.0135224

[13] Eschen, W., Loetgering, L., Schuster, V., Klas, R., Kirsche, A., Berthold, L., . . . , & Rothhardt, J. (2022). Material-specific high-resolution table-top extreme ultraviolet microscopy. *Light: Science & Applications*, *11*(1), 117. https://doi.org/10.1038/s41377-022-00797-6

[14] Porfirev, A., Khonina, S., & Kuchmizhak, A. (2023). Light–matter interaction empowered by orbital angular momentum: Control of matter at the micro- and nanoscale. *Progress in Quantum Electronics*, *88*, 100459. https://doi.org/10.1016/j.pquantelec.2023.100459

[15] Trichili, A., Park, K. H., Zghal, M., Ooi, B. S., & Alouini, M. S. (2019). Communicating using spatial mode multiplexing: Potentials, challenges, and perspectives. *IEEE Communications Surveys & Tutorials*, *21*(4), 3175–3203. https://doi.org/10.1109/COMST.2019.2915981

[16] Feng, Q., Kong, X., Shan, M., Lin, Y., Li, L., & Cui, T. J. (2022). Multi-orbital-angular-momentum-mode vortex wave multiplexing and demultiplexing with shared-aperture reflective metasurfaces. *Physical Review Applied*, *17*(3), 034017. https://doi.org/10.1103/PhysRevApplied.17.034017

[17] Liu, Y., Rishøj, L. S., Galili, M., Ding, Y., Oxenløwe, L. K., & Morioka, T. (2021). Data transmission using orbital angular

momentum mode multiplexing and wavelength division multiplexing with a silicon photonic integrated MUX chip. In *2021 European Conference on Optical Communication*, 1–4. https://doi.org/10.1109/ECOC52684.2021.9606096

[18] Chen, S., Li, S., Fang, L., Wang, A., & Wang, J. (2019). OAM mode multiplexing in weakly guiding ring-core fiber with simplified MIMO-DSP. *Optics Express*, *27*(26), 38049–38060. https://doi.org/10.1364/OE.27.038049

[19] Fang, J., Li, J., Kong, A., Xie, Y., Lin, C., Xie, Z., . . . , & Yuan, X. (2022). Optical orbital angular momentum multiplexing communication via inversely-designed multiphase plane light conversion. *Photonics Research*, *10*(9), 2015–2023. https://doi.org/10.1364/PRJ.458474

[20] Porfirev, A. P., Logachev, V. I., Gridin, G. E., Kirilenko, M. S., & Fomchenkov, S. A. (2020). Nonlinear spiral phase plates for generation of light fields with orbital angular momentum. In *Optical Technologies for Telecommunications 2019: Proceedings of SPIE*, *11516*, 115160A. https://doi.org/10.1117/12.2553206

[21] Jankowski, T., Bennis, N., Morawiak, P., Zografopoulos, D. C., Pakuła, A., Filipiak, M., . . . , & Algorri, J. F. (2024). Optical vortices by an adaptive spiral phase plate. *Optics & Laser Technology*, *176*, 111029. https://doi.org/10.1016/j.optlastec.2024.111029

[22] Lian, Y., Qi, X., Wang, Y., Bai, Z., Wang, Y., & Lu, Z. (2022). OAM beam generation in space and its applications: A review. *Optics and Lasers in Engineering*, *151*, 106923. https://doi.org/10.1016/j.optlaseng.2021.106923

[23] Khonina, S. N., Ustinov, A. V., Logachev, V. I., & Porfirev, A. P. (2020). Properties of vortex light fields generated by generalized spiral phase plates. *Physical Review A*, *101*(4), 043829. https://doi.org/10.1103/PhysRevA.101.043829

[24] Zheng, S., Zhao, Z., & Zhang, W. (2023). Versatile generation and manipulation of phase-structured light beams using on-chip subwavelength holographic surface gratings. *Nanophotonics*, *12*(1), 55–70. https://doi.org/10.1515/nanoph-2022-0513

[25] Liu, A., Wu, M., Zhuang, R., Hong, J., Wang, Q., & Ren, X. (2020). On-chip generation of the reconfigurable orbital angular momentum with high order. *Optics Express*, *28*(12), 17957–17965. https://doi.org/10.1364/OE.393320

[26] Maji, S., & Brundavanam, M. M. (2018). Topological transformation of fractional optical vortex beams using computer generated holograms. *Journal of Optics*, *20*(4), 045607. https://doi.org/10.1088/2040-8986/aab1da

[27] Cognée, K. G., Doeleman, H. M., Lalanne, P., & Koenderink, A. F. (2020). Generation of pure OAM beams with a single state of polarization by antenna-decorated microdisk resonators. *ACS Photonics*, *7*(11), 3049–3060. https://pubs.acs.org/doi/10.1021/acsphotonics.0c01081

[28] Koley, A., & Tripathi, S. M. (2024). Bi-directional high-order orbital angular momentum mode generation using gratings in high numerical aperture fiber. *Journal of Optics*, *26*(4), 045605. https://doi.org/10.1088/2040-8986/ad2a23

[29] Wang, J., Shao, Z., Wen, Y., Qiu, X., Chen, Y., Zhang, Y., . . . , & Chen, L. (2019). All-dielectric metasurface grating for on-chip multi-channel orbital angular momentum generation and detection. *Optics Express*, *27*(13), 18794–18802. https://doi.org/10.1364/OE.27.018794

[30] Yang, Y., Li, H., Liu, H., & Chen, X. (2023). Highly efficient nonlinear vortex beam generation by using a compact nonlinear fork grating. *Optics Letters*, *48*(24), 6376–6379. https://doi.org/10.1364/OL.506901

[31] Zhao, H., Wang, P., Yamakawa, T., & Li, H. (2019). All-fiber second-order orbital angular momentum generator based on a single-helix helical fiber grating. *Optics Letters*, *44*(21), 5370–5373. https://doi.org/10.1364/OL.44.005370

[32] Bernas, M., Zolnacz, K., Napiorkowski, M., Statkiewicz-Barabach, G., & Urbanczyk, W. (2021). Conversion of LP_{11} modes to vortex modes in a gradually twisted highly birefringent optical fiber. *Optics Letters*, *46*(18), 4446–4449. https://doi.org/10.1364/OL.433952

[33] Wong, G. K. L., Kang, M. S., Lee, H. W., Biancalana, F., Conti, C., Weiss, T., & Russell, P. S. J. (2012). Excitation of orbital angular momentum resonances in helically twisted photonic crystal fiber. *Science*, *337*(6093), 446–449. https://doi.org/10.1126/science.1223824

[34] Lu, J., Meng, L., Shi, F., Liu, X., Luo, Z., Yan, P., . . . , & Zhou, P. (2018). Dynamic mode-switchable optical vortex beams using acousto-optic mode converter. *Optics Letters*, *43*(23), 5841–5844. https://doi.org/10.1364/OL.43.005841

[35] Zhang, W., Huang, L., Wei, K., Li, P., Jiang, B., Mao, D., . . . , & Zhao, J. (2016). High-order optical vortex generation in a few-mode fiber via cascaded acoustically driven vector mode conversion. *Optics Letters*, *41*(21), 5082–5085. https://doi.org/10.1364/OL.41.005082

[36] Li, S., Mo, Q., Hu, X., Du, C., & Wang, J. (2015). Controllable all-fiber orbital angular momentum mode converter. *Optics Letters*, *40*(18), 4376–4379. https://doi.org/10.1364/OL.40.004376

[37] Liu, Z., Zhu, G., Li, Y., Yu, J., Bai, Z., Liu, S., . . . , & Wang, Y. (2020). Orthogonal long-period fiber grating for directly exciting the orbital angular momentum. *Optics Express*, *28*(18), 27044–27051. https://doi.org/10.1364/OE.399929

[38] Zhao, Y., Wang, C., Liu, Z., Zhou, K., Mou, C., Liu, Y., . . . , & Wang, T. (2017). Generation of multiple-order OAM modes using a tilted few-mode fiber Bragg grating. In *Asia Communications and Photonics Conference,* S3A.3. https://doi.org/10.1364/ACPC.2017.S3A.3

[39] Li, Y., Bai, Z., Liu, Z., Zhu, G., Yang, K., Yu, J., . . . , & Wang, Y. (2020). High purity optical vortex generation in a fiber Bragg grating inscribed by a femtosecond laser. *Optics Letters*, *45*(24), 6679–6682. https://doi.org/10.1364/OL.410277

[40] Liu, R., Li, Y., Chen, J., Wu, L., Ran, J., Chen, Z., . . . , & Wang, Y. (2022). Direct generation of orbital angular momentum in orthogonal fiber Bragg grating. *Optics Express*, *30*(16), 28745–28751. https://doi.org/10.1364/OE.467491

[41] Yang, K., Liu, Y., Wang, Z., Li, Y., Han, Y., Zhang, H., & Mao, B. (2020). Triple-order orbital-angular-momentum modes generation based on single tilted fiber Bragg grating in a few-mode ring-core fiber. *Optical Fiber Technology*, *55*, 102155. https://doi.org/10.1016/j.yofte.2020.102155

[42] Okhrimchuk, A. G., Likhov, V. V., Vasiliev, S. A., & Pryamikov, A. D. (2022). Helical Bragg gratings: Experimental verification of light orbital angular momentum conversion. *Journal of Lightwave Technology*, *40*(8), 2481–2488. https://doi.org/10.1109/JLT.2021.3137055

[43] Detani, T., Zhao, H., Wang, P., Suzuki, T., & Li, H. (2021). Simultaneous generation of the second-and third-order OAM modes by using a high-order helical long-period fiber grating. *Optics Letters*, *46*(5), 949–952. https://doi.org/10.1364/OL.418248

[44] Wang, Y., Liu, Y., Zhao, W., Yang, J., Geng, W., Fang, Y., . . . , & Yue, Y. (2022). Multi-ring-air-core fiber supporting numerous radially fundamental OAM modes. *Journal of Lightwave Technology*, *40*(13), 4420–4428. https://doi.org/10.1109/JLT.2022.3162852

[45] Tu, J., Wu, J., Huang, C., Zhang, J., Gao, S., Liu, W., & Li, Z. (2023). OAM mode generation in helically twisted hollow-core

antiresonant fiber. *Optics Letters*, *48*(7), 1634–1637. https://doi.org/10.1364/OL.485302

[46] Koley, A., & Tripathi, S. M. (2021). Sensing characteristics of grating assisted counterpropagating cladding modes in optical fibers. *Applied Optics*, *60*(29), 9129–9137. https://doi.org/10.1364/AO.434757

[47] Kashyap, R. (2010). *Fiber Bragg gratings* (2nd ed.). USA: Elsevier. https://doi.org/10.1016/C2009-0-16830-7

[48] Li, Y., Jin, L., Wu, H., Gao, S., Feng, Y. H., & Li, Z. (2017). Superposing multiple LP modes with microphase difference distributed along fiber to generate OAM mode. *IEEE Photonics Journal*, *9*(2), 1–9. https://doi.org/10.1109/JPHOT.2017.2674022

[49] Snyder, A. W., & Love, J. D. (1983). *Optical waveguide theory*. USA: Springer. https://doi.org/10.1007/978-1-4613-2813-1

[50] Okamoto, K. (2006). *Fundamentals of optical waveguides* (2nd ed.). USA: Academic Press. https://doi.org/10.1016/B978-0-12-525096-2.X5000-4

[51] McGloin, D., Simpson, N. B., & Padgett, M. J. (1998). Transfer of orbital angular momentum from a stressed fiber-optic waveguide to a light beam. *Applied Optics*, *37*(3), 469–472. https://doi.org/10.1364/AO.37.000469

[52] Erdogan, T. (1997). Cladding-mode resonances in short- and long-period fiber grating filters. *Journal of the Optical Society of America A*, *14*(8), 1760–1773. https://doi.org/10.1364/JOSAA.14.001760

How to Cite: Koley, A. (2025). Fiber Bragg Grating-Based Tunable Wavelength Orbital Angular Momentum Beam Generation with Varying Polarization. *Journal of Optics and Photonics Research*, *2*(2), 67–76. https://doi.org/10.47852/bonviewJOPR42022826